

We are IntechOpen, the world's leading publisher of Open Access books Built by scientists, for scientists

6,900

Open access books available

186,000

International authors and editors

200M

Downloads

Our authors are among the

154

Countries delivered to

TOP 1%

most cited scientists

12.2%

Contributors from top 500 universities



WEB OF SCIENCE™

Selection of our books indexed in the Book Citation Index
in Web of Science™ Core Collection (BKCI)

Interested in publishing with us?
Contact book.department@intechopen.com

Numbers displayed above are based on latest data collected.
For more information visit www.intechopen.com



Raman Microscopy: A Suitable Tool for Characterizing Surfaces in Interaction with Plasmas in the Field of Nuclear Fusion

Cedric Pardanaud, Celine Martin and
Pascale Roubin

Additional information is available at the end of the chapter

<http://dx.doi.org/10.5772/65649>

Abstract

Raman microscopy, which is sensitive to chemical bonds, defects, structure, is a suitable tool that can give information on how a material can be modified by interacting with ions. We will first give concrete examples on how it can be used to characterize with a micrometric resolution samples extracted from tokamaks. We will then give concrete examples on what information can be obtained by doing a study on laboratory synthesized materials, benchmarking Raman microscopy with quantitative techniques. The first part of the chapter is focused on carbon-based material analysis. We will show how Raman spectra are sensitive to the presence of hydrogen, a major safety issue in the field. The second part of the chapter will be focused on beryllium- and tungsten-based material analysis. We will show that hydrogen can be stored as an hydride after ion implantation and that it can be released easily in tungsten oxide.

Keywords: plasma wall interaction, hydrogen isotope implantation, carbon, beryllium, tungsten

1. Introduction

Raman microscopy, which is sensitive to chemical bonds, defects, and structure, is a suitable tool that can give information on how a material can be modified by interacting with ions. We first gave concrete examples on how it can be used to characterize with a micrometric resolution samples extracted from tokamaks. We then gave concrete examples on what information can be obtained by doing a study on laboratory-synthesized materials, comparing

Raman microscopy with quantitative techniques. The first part of the chapter is focused on carbon-based material analysis. We showed how Raman spectra are sensitive to the presence of hydrogen, a major safety issue in the field. The second part of the chapter is focused on beryllium- and tungsten-based material analysis. We showed that hydrogen can be stored as a hydride after ion implantation and that it can be released easily in tungsten oxide.

1.1. Plasma-wall interactions in tokamaks

Tokamaks are machines made to study the possibility to make energy from nuclear fusion reactions by confining hot plasma (1–100 keV ions) magnetically. The future international reactor *ITER*¹ (International Thermonuclear Experimental Reactor), now in construction at Cadarache (south of France), is one of them. One of its aims is to produce, with the help of the D+T nuclear reaction, 500 MW by injecting 50 MW. The D+T nuclear reaction has been chosen because it has the highest cross section in the relevant domain of energy (one to two orders of magnitudes higher than the D+D reactions). The D+T reaction will produce 14-MeV neutrons and 3.52-MeV He nuclei, which will maintain the temperature of the D+T reacting plasma to an equilibrium state. Magnetic field lines are however connected to the inner walls of the ITER torus, which leads to the existence of cold edge plasma (composed of He, D, T, impurities such as oxygen or eroded metals) interacting with them. The heat produced by the hot plasma is received mainly on a part of the wall called a *divertor*. The material that will compose this part will have to work with heat loads in the range 10–20 MW/m².

Then, in tokamaks, understanding and being able to predict the evolution of the plasma-facing components (PFCs) that interact with both heat loads and the cold edge plasma is one of the keystones to make nuclear fusion a way of producing energy in the future [2]. The material chosen for the *divertor* is tungsten as it drives well the heat to the underlying cooling loops present in the PFCs, it is difficult to erode, and its melting/fusion temperatures are very high, and hence creating bonding with hydrogen isotope is supposed to be difficult. The other parts of the PFCs are composed of beryllium [3]. Some tokamaks are already working nowadays in an ITER-like wall (ILW) configuration to prepare the ITER project, such as the Joint European Torus/JET tokamak, with some PFCs composed of tungsten-coated carbon tiles [4–6], carbon tiles, mounted on *limiters* and/or *neutralizers*, being used in the ancient carbon area of tokamaks, now abandoned, because of tritium retention (tritium being radioactive and being easily trapped in carbon) [7, 8]. In that framework, the surface composition and morphology modifications under operation will lead to changes in the material properties that can address safety issues. These changes will have to be measured and then understood. In more details, the migration [9] and/or melting of elements in the machine [10, 11], the production of dust, the hydrogen isotope retention [12, 13], the impurity contamination (traces of carbon and/or oxygen, nitrogen seeding [14], etc.) leading to formation of new mixed materials/phases (such as oxides or alloys) and the complex surface erosion will all influence the lifetime of these PFCs and their fuel retention properties. Surface characterization techniques are then necessary to measure the elemental changes in JET and in ITER PFCs erosion zones and deposits.

¹To give an idea of the size of the project and the machine: the tokamak alone will stay in a room which is 60 m high, all the site will be sprayed on a surface which is 420,000 m² and the machine itself weighed 23,000 tons [1].

1.2. Raman microscopy as a technique to probe the top of deposits

In this field of research, due to their isotope selectivity, ion beam analyses (IBA) play a prominent role in this characterization, as discussed in Refs. [15, 16]. Thermal desorption spectroscopy (TDS) also plays a key role as it can give access to the characterization of D or T trap energies in metals such as Be [17–19] or W [20]. However, even if TDS and IBA techniques give quantitative information about hydrogen isotope concentration, they only give indirect information about chemical bonding. A direct way to probe that chemical bondings is to probe them spectroscopically by means of their vibrational spectrum using Raman microscopy.

Moreover, the in-depth resolution reached by IBA is not enough to describe properly the top layer of deposits called the *hydrogen isotope supersaturated layer*, which sizes in the range of tens of nanometers, and is composed of few atomic percent to few tens of atomic percent of hydrogen isotopes [13]. Depending on the material, Raman microscopy can be a well-suited technique adapted to that depth, as can be seen in **Figure 1**. In that figure, the transmittance coding the effectiveness of a material in transmitting incident light is plotted for $\lambda_L = 514$ nm and for Be, W, C (graphite and amorphous form). The depth at which the transmitted energy reaches 10% of the initial incident energy is 30, 35, 70 and 310 nm for, respectively, Be, W, C\graphite and amorphous carbon. The last value depends on the local organization of the amorphous structure, as detailed in Refs. [21–23]. Note that as the Raman measurements are generally done in back scattering geometry, one has to take into account an additional factor 2 in the argument of the exponential, as mentioned in [21, 22].

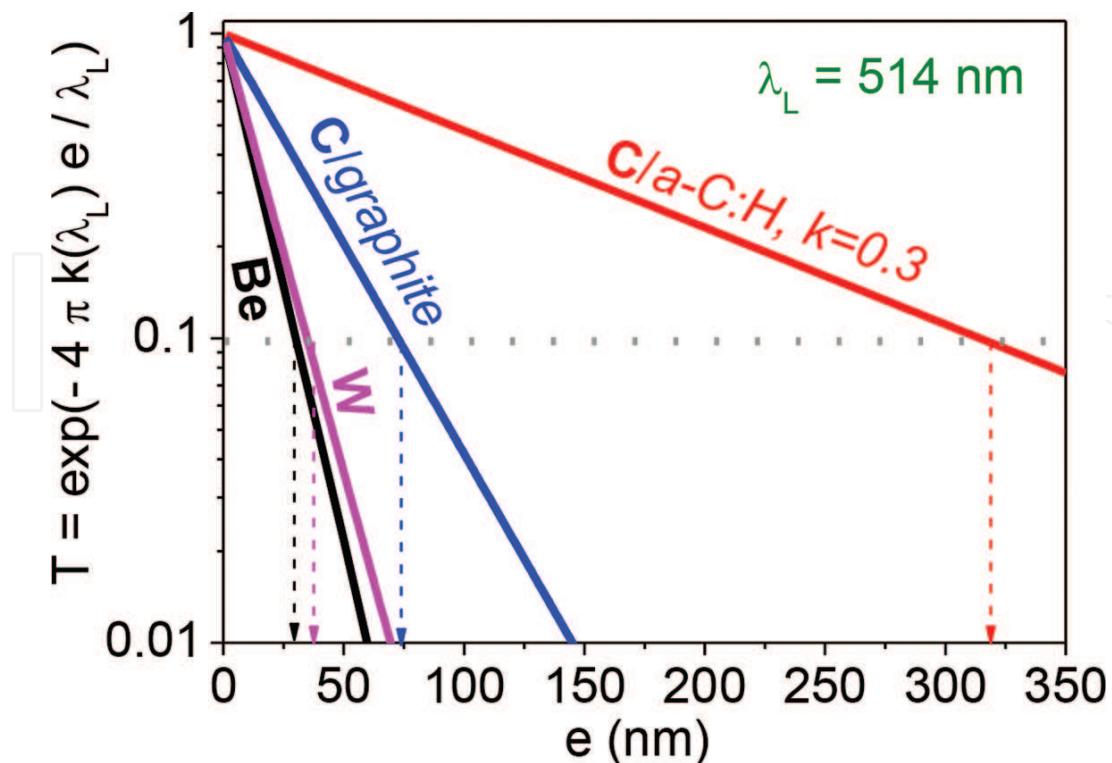


Figure 1. Transmittance in function of the depth for Be, W, C.

The aim of this chapter is to give concrete examples on how Raman microscopy can be used to characterize samples extracted from tokamaks, from the micrometric to the macroscopic scale of the machine. We then gave concrete examples on what information can be obtained by doing a study on laboratory-synthesized materials, benchmarking Raman microscopy with quantitative techniques such as TDS or IBA. The first part of the chapter is focused on carbon-based material analysis as all the previous tokamaks were using this element in the past. We showed how Raman spectra are sensitive to the presence of hydrogen, a major safety issue in the field. The second part of the chapter is focused on beryllium and tungsten based material analysis. We showed that hydrogen can be stored as a hydride after ion implantation, and that it can be released easily in tungsten oxide.

2. Carbon materials

2.1. Context

The Tore Supra tokamak had the ability to perform long plasma discharges with actively cooled PFC, which was a good opportunity to study fuel retention, a major concern in the plasma-wall interaction community. The study devoted to that was the Deuterium Inventory in Tore Supra (DITS) campaign. It was aimed at studying and linking the erosion of carbon PFCs and the fuel retention. The in-vessel D inventory was followed after the D loading campaign through particle balance [24], a part of the toroidal pump limiter (TPL), which was actively cooled during discharges, was dismantled for an extensive postmortem analysis of a few tens of carbon fiber composite tiles (CFC). The TPL was situated on top of a part of the machine called the neutralizer (NTR), which was also composed of CFC, but which was not actively cooled during discharges.

The *post-mortem* analyses used techniques devoted to the estimation of the D inventory [25, 26] and to structural and chemical characterizations [27], Raman microscopy being one of them [26, 28, 29]. Due to the different rates of erosion/deposition associated to the plasma footprint, the TPL surface exhibited a pattern which combined deposition-dominated zones (labeled thick and thin depending on the amount of matter found) and erosion-dominated zones. The shapes of these patterns were reproduced by simulating plasma wall interactions from the micrometric to the metric scale [30, 31].

Temperatures of the TPL were determined (with the help of thermographic measurements [24]) to be 500°C for gap surfaces of both thick deposit tiles and eroded tiles, 200°C for top surfaces of eroded tiles and 120°C for both gap and top surfaces of CFC tiles situated in the so-called thin deposit region. Temperature was estimated to vary in the range 500–900°C for the top surface of thick deposit tiles.

In **Figure 6**, we display Raman spectroscopic parameters of several samples, but before detailing the figure, we need to remember some well-known facts about the Raman

spectroscopy of disordered and amorphous carbons. They are briefly given below but are not detailed.

Raman microscopy is routinely used to characterize rapidly C-based materials, from nano-crystalline graphite (nc-G) to amorphous carbons, hydrogenated or not (a-C:H or a-C). It probes the structure [32] and is highly sensitive to bonding properties by interpreting the 1000–1800 cm^{-1} region, dominated by the G and D bands due to $\text{C}(\text{sp}^2)$ hybridization of carbon atoms [33]. The G band, close to $\sigma_{\text{G}}=1600 \text{ cm}^{-1}$, is assigned to the bond stretching of both aromatic and aliphatic C-C pairs, whereas the D band, close to 1350 cm^{-1} with a 514-nm laser (associated with a D' band close to 1620 cm^{-1}) is assigned to the breathing mode of aromatic rings. The Raman analysis of graphite and nc-G clearly shows that this D band exists only when there is disorder [32]. Implanted graphite also displays this D band [34]. For a-C and a-C:H, the G bandwidth is related to disorder (sp^2 cluster size, cluster size distribution, chemical bonding) or stress [35] and presence of $\text{C}(\text{sp}^3)$. For disordered multilayer graphene, the G bandwidth evolution can also be related to disorder [36].

Spectra of a-C and nc-G are clearly distinct [37] (spectrum 1 from **Figure 8(a)** belongs to a-C, whereas spectrum 3 belongs to nc-G, whereas spectrum 2 is in between): for example, G and D bands are much broader for a-C (width $\Gamma_{\text{G}} \sim 80\text{--}200 \text{ cm}^{-1}$) than for nc-G (width ~ 15 to 40 cm^{-1}). Moreover, the intensity ratio (D over G band intensity) depends on the amount of disorder. Generally, to reproduce experimental nc-G spectra, bands at $\sim 1500 \text{ cm}^{-1}$ and at $\sim 1200 \text{ cm}^{-1}$ are very often needed, interpreted as sp^3 or out-of-plane defects, or as an additional amorphous contribution [38–43], see the discussions in Refs. [29, 43]. Raman spectra thus contain information on disorder [35] such as the size clusters, L_{a} [32, 44], the $\text{C}(\text{sp}^2)/\text{C}(\text{sp}^3)$ ratio, the hydrogen content [45–47], etc. All these information will help trying to understand the complex thermo/chemistry story of samples extracted from tokamaks.

2.2. Laboratory experiments

2.2.1. H-content determination in a-C:H layers

The Raman parameters generally used to probe the structure are the peak wavenumber and the width of the G and D bands, respectively, and the peak height ratio of these two bands, $H_{\text{D}}/H_{\text{G}}$ [48]. An additional spectral feature has to be taken into account: a photoluminescence background which is superimposed to the Raman spectrum and is correlated to the H content [46]. The slope of this background, m , is calculated between 800 and 2000 cm^{-1} . The higher m , the higher is the photoluminescence intensity. **Figure 2** displays ultra-high vacuum heating effect on a 220-nm thick hard amorphous, hydrogenated carbon thin films (a-C:H) that were deposited on a Si [49]. The mass density of such typical hard a-C:H layers, with H/H+C ~ 30 at.% is $\sim 1.9 \text{ g cm}^{-3}$ are formed [50].

Figure 2 displays the thermal evolution of m/H_{G} and $H_{\text{D}}/H_{\text{G}}$ compared to the H content determined by IBA and the H_2 release determined by TPD. σ_{G} is not shown here but it reaches a plateau for $T > 600^\circ\text{C}$, meaning that the number of $\text{C}(\text{sp}^3)$ neighboring $\text{C}(\text{sp}^2)$ no longer changes.

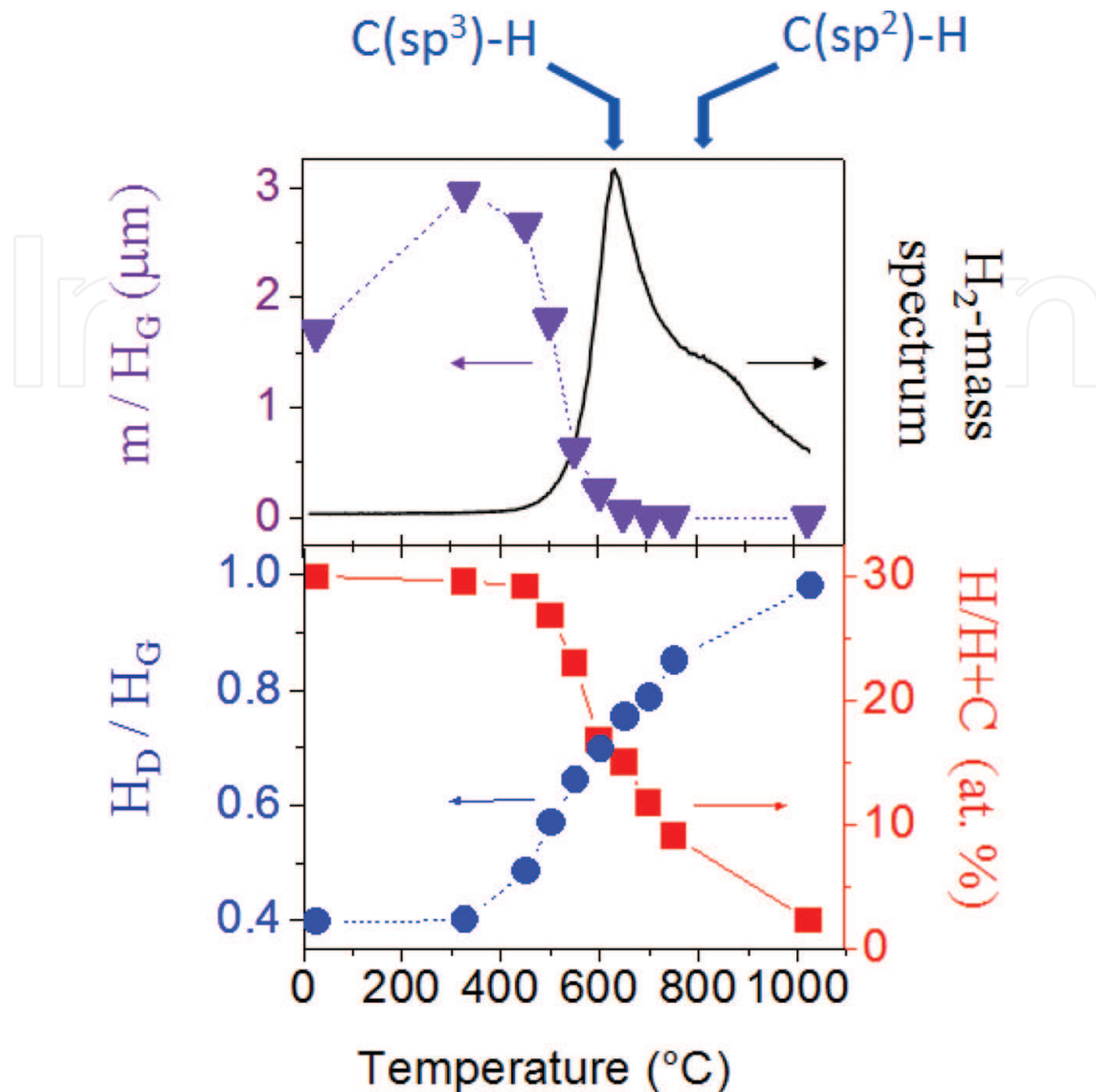


Figure 2. TDS, IBA and Raman microscopy measurements of a heated a-C:H sample.

We see that m/H_G increases by $\sim 40\%$ between room temperature and 300°C , decreasing between 300 and 600°C (at that point, $m/H_G \sim 0.05$). For $T > 600^\circ\text{C}$, the slope is close to zero. If we compare to the H content, between RT and 300°C , it is constant ($\text{H}/\text{H}+\text{C} \sim 30 \text{ at.}\%$). Then, the increase of the m/H_G spectroscopic parameter is due to aromatization (and defect passivation) that leads to an increase of the photoluminescence background. As a consequence, m/H_G cannot be related easily to $\text{H}/\text{H}+\text{C}$ in this thermal range. For higher temperatures, the H content decreases from 30 down to approximately 2%, without reaching a plateau.

The bottom part of **Figure 2** shows that H_D/H_G and $\text{H}/\text{H}+\text{C}$ evolve in a remarkably symmetrical way. This suggests that the two parameters are correlated and that H_D/H_G could be used to probe the hydrogen content. The relation obtained that works with a 514 nm laser is ($\text{H}/\text{H}+\text{C} = 0.54 - 0.53 H_D/H_G$) in the range $\text{H}/\text{H}+\text{C} = 2-30 \text{ at.}\%$. Such a linear law, with the same slope, can be obtained for other wavelengths (407–633 nm has been tested), but with a different value at the origin.

2.2.2. Long-term hydrogen release revealed by in situ Raman spectroscopy

The thermal stability of six 200-nm-thick plasma enhanced chemical vapor deposited a-C, a-C:H and a-C:D layers ranging from soft to hard layers has been studied. The imaginary part of the refractive index at 633 nm and the corresponding H or D contents have been displayed together and compared to results from the literature [50], showing a good agreement with what is known: when the H content increases, the sample becomes more transparent, because of the diminution of aromatic C(sp²) bonds. **Figure 3(b)** displays the thermal evolution of H_D/H_G for these six samples heated with a linear ramp (3°C min⁻¹) under a 1-bar argon atmosphere from room temperature to 600°C. Without entering into details, that can be found in [23], let us only focus on H data. One can see that the more hydrogen there is on the as deposited sample, at a lower temperature, the H_D/H_G ratio starts to increase. Because the evolution of H_D/H_G for a H-free amorphous carbon is small and because of what was shown in the previous part, most of the evolution in that thermal range is due to hydrogen release from C(sp³). This is consistent with what is known in the literature about the bad thermal stability of hydrogen-rich a-C [51–55].

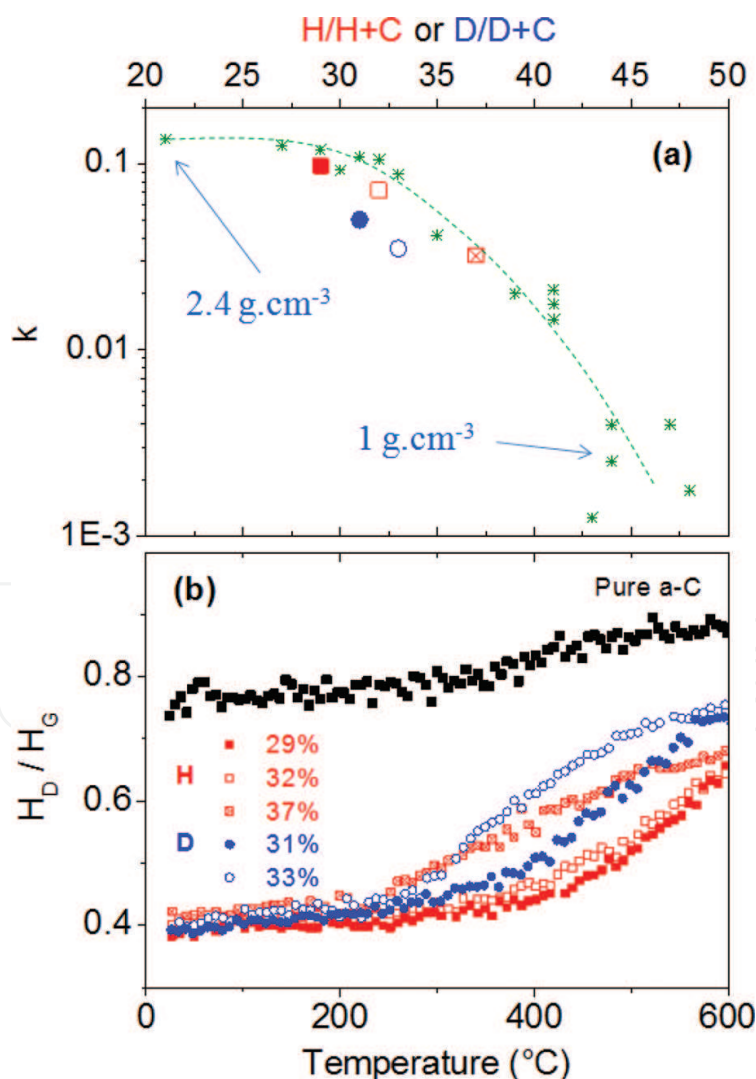


Figure 3. Thermal evolution of HD/HG for six a-C samples. (a) Optical constant in function of H content. (b) Comparative linear ramp study. Green stars in the top figure are from Ref. [50].

Figure 4 displays an example of isothermal evolution in function of time. This evolution cannot be due to the effect of the laser on the sample, accumulating heat with long times, as we compared two sets of data: one by switching off the laser between acquisitions and one with a continuous flux of heat. The position of the G band (not shown) no more evolves after 50 min, meaning there is no order increase due to an overestimated heat load by the probe laser. In Ref. [56], we studied that we had no power dependence in the range $0.01\text{--}1\text{ mW}/\mu\text{m}^2$. Then, this technique allows to probe long-term hydrogen release. We will use it on tokamak samples in Section 2.3.

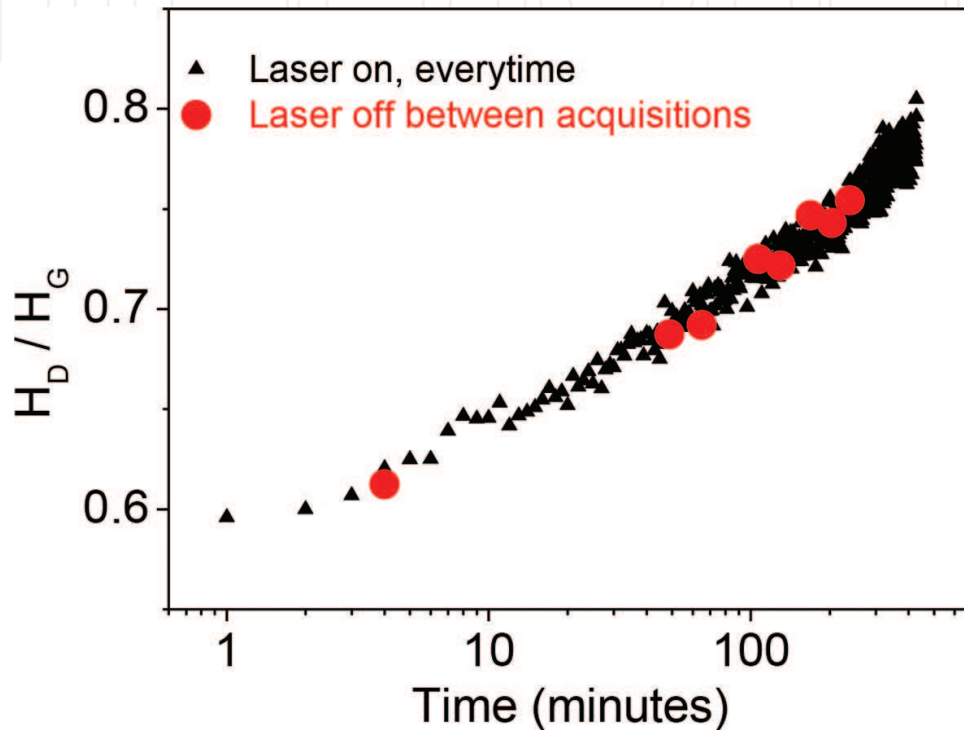


Figure 4. Example of in situ measurement isothermal annealing.

Then, to resume, we have shown that

- The m/H_C parameter, often used to estimate the H content in the literature, should be used with care, first because it is sensitive to various photoluminescence-quenching processes and second because it is not sensitive to H bonded to $C(sp^2)$.
- The H_D/H_C parameter is quasi-linear in the full range of H content and can thus be used to estimate the H content.
- H_D/H_C can be used in situ to retrieve the H content evolution under heating.

2.2.3. H, D and He implantation in graphite: Starting the amorphization regime

The modification by ion impact of graphite has been studied both theoretically and experimentally ([57–67] and references therein). Inside the sample, collision cascades are created by ions that knock on the surface and penetrate. It creates defects and vacancies, ions being implanted

after they slow down [68]. Protusions (height lower than 1 nm), called hillocks, are observed for low fluencies ($<10^{14}$ ions cm^{-2}) [57, 58]. They are due to stress created by the first collision under the near surface region. More precisely, interstitial carbon clusters or coalescence of interstitials and vacancies are at the origin of these hillocks. At fluencies $>10^{15}$ ions cm^{-2} [61, 62] and in the 400–800 K range, domes with a height one order of magnitude higher were observed.

We have exposed graphite to hydrogen deuterium and helium plasma (from 10^{16} to 10^{18} cm^{-2}) [43]. The energies were tuned from 40 to 800 eV. The ion incidence was parallel to the basal plane for CFC (carbon/carbon composite) and perpendicular for HOPG (highly oriented pyrolytic graphite). The changes of the material were studied by means of both Raman and atomic force microscopies.

We display the 400 eV/D implantation Raman spectra in **Figure 5** as an illustration. The main differences or common points between HOPG and CFC are

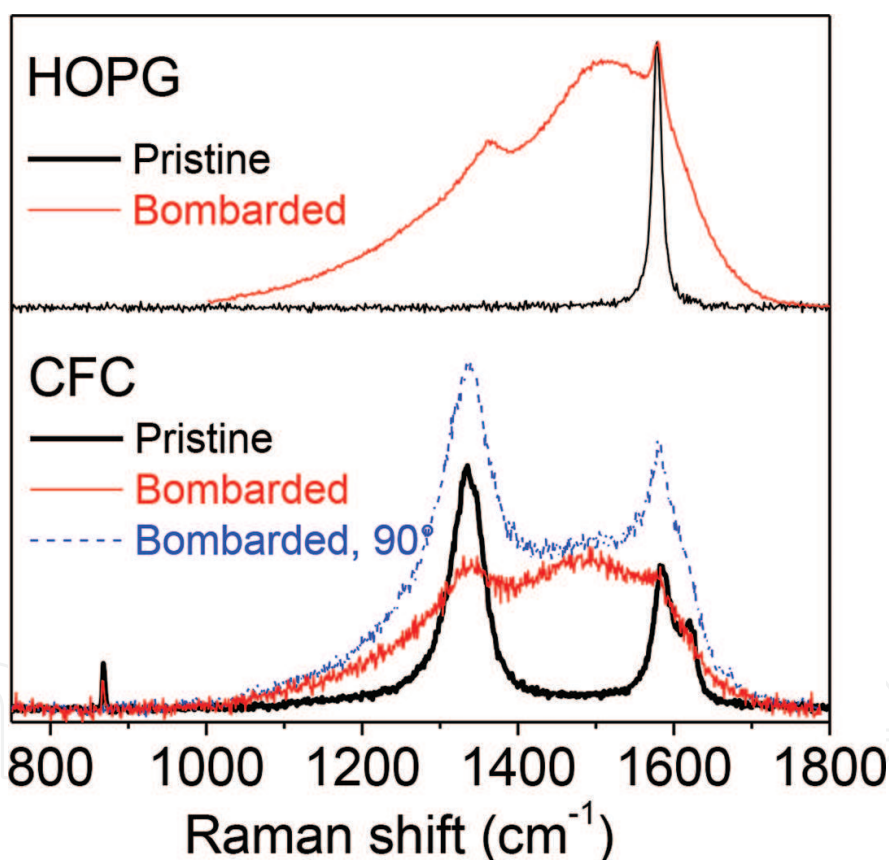


Figure 5. Raman spectra of bombarded HOPG and CFC.

- Pristine HOPG contains less defects than CFC (D band at 1350 cm^{-1} is close to zero for HOPG, whereas H_D/H_C is close to 2 for CFC, indicating nanometric crystal size domains)
- Implantation produces an amorphization for both materials (broad bands at $1500\text{--}1300\text{ cm}^{-1}$ appearing in the spectra, looking like the spectrum 1 in **Figure 8(a)**)

- The underlying pristine sample is visible can be seen in both cases. This is because the ions penetrate only 15–20 nm and the penetration depth of light is few tens of nanometer (see **Figure 1**).
- Both bombarded Raman spectra display two kind of environment: in-plane defects and out of plane defects (see Ref. [43] for details).
- No laser probe polarization effect of IPD and OPD on the HOPG sample, whereas there is one for IPD of the CFC.

When increasing the impinging ion energy, the growth of nanometric domes at the surface has been observed by atomic force microscopy (AFM) and the incident kinetic energy has been found as the parameter determining their height. The Raman study has also revealed that both the defect-defect distance in the IPD and OPD are typically 1 nm. When the number of vacancies created in the material increases, the number of in-plane defects decreases to the benefit of the out-of-plane defects.

2.3. Information retrieved from tokamak samples

2.3.1. Raman measurements inside the tokamak Tore Supra

Figure 6 displays the G band position, σ_G in function of its width, Γ_G for many samples collected in the Tokamak Tore Supra (deposition zones and erosion zones of the TPL, and on the NTR) and compared to pristine CFC and to heated laboratory deposited a-C:H (see Sect. 2.2 of this chapter for more information). The data points form a wide range of carbon materials from nc-G to a-C, all described in more details in [28, 69, 70]. Pristine CFC data points are all situated at $\Gamma_G \sim 25 \text{ cm}^{-1}$ and $\sigma_G \sim 1580 \text{ cm}^{-1}$. NTR deposits form a data point cloud continuously spread either along the positive slope straight line (Γ_G in the range 20–80 cm^{-1} , σ_G in the range 1580–1600 cm^{-1}) or along the negative slope straight line for the TPL deposited and eroded samples (Γ_G in the range 80–180 cm^{-1} , σ_G in the range 1600–1520 cm^{-1}). The deposited TPL points are very close to a-C:H data points, at slightly lower frequency. Note that the shift between heated a-C:H and the TPL deposits can be attributed to an isotopic effect as TS samples are deuterated samples, which downshifts the G band position. A proof of that can be found in Ref. [23] where both synthetic a-C:H and a-C:D were heated and compared. The a-C:H data were heated under vacuum from room temperature (right down corner up to 1000°C, left up corner). Then this line from right to left means that the carbons locally organize under heating. This is in agreement with the temperature measured in situ by thermography. The NTR deposits display lower Γ_G values, meaning they are more structured. This is in agreement with the fact that the NTR was not actively cooled, being able to reach temperatures higher than 1000°C. As it is known that the deuterium is released at these temperatures (see Section 2.2 of this chapter, below), one can say that the D is mainly trapped in deposits found on the TPL and not on the NTR. The eroded TPL samples are less spread than the others, meaning the structure of the implanted carbons is more homogeneous and more amorphous. It can retain more deuterium, relatively. However, the thickness of that layer was found to be few nanometers only [69], which is low compared to the hundreds of microns found for Tore Supra deposits, meaning the D is essentially trapped in these deposits or deeper in the porosities of the initial pristine CFC. These points are investigated in a next subpart.

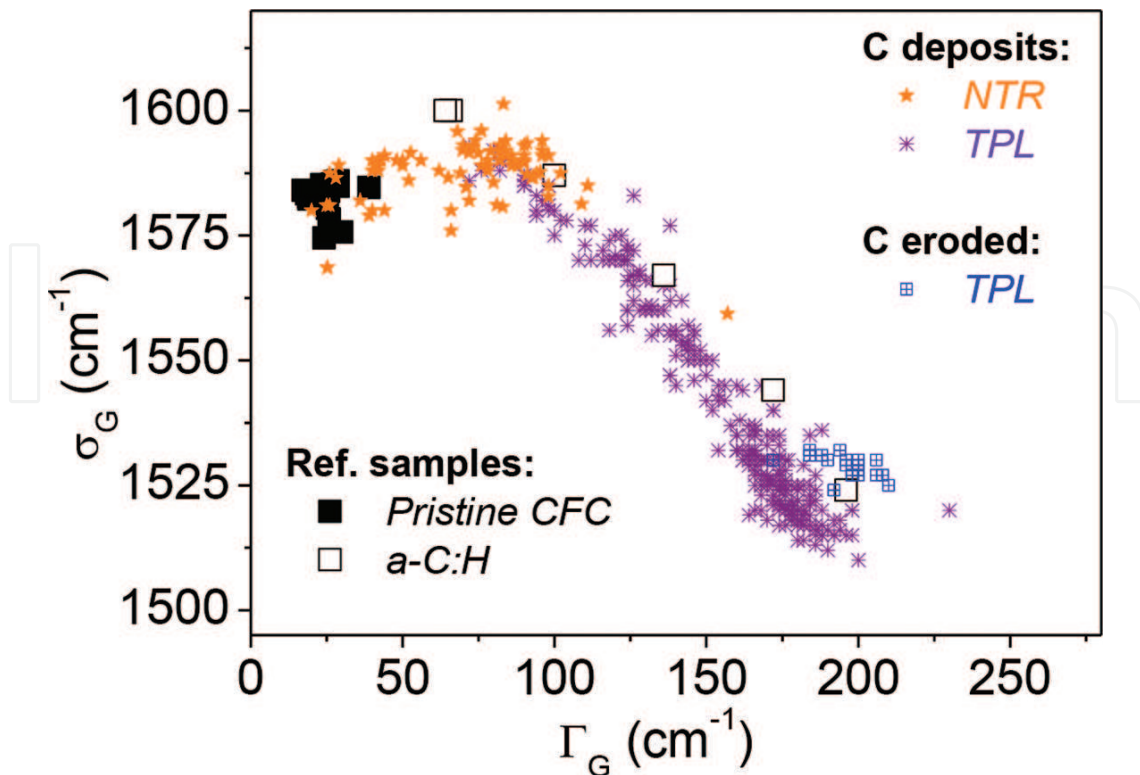


Figure 6. Carbon deposits spectroscopic parameters: G band position in function of its full width at half maximum.

2.3.2. Micrometric inhomogeneities and long-term release of H

In Ref. [23], we compared with Raman microscopy the thermal evolution of reference samples to samples extracted from the Tore Supra tokamak, as it was shown that a long-term mechanism [71] occurred even at low temperature (low means here 120°C, which correspond to the thermostat temperature of the PFC cooling loop, staying at this values for days and weeks even when the plasma is off) and as we wanted to distinguish the Raman signature of this heating. **Figure 7** displays the Raman data of the Tore Supra samples. **Figure 7(a)** and **(b)** is mappings of m/H_G and s_G , respectively, for an as received sample. One can see that the deposit is inhomogeneous, the sample being more organized in the upper right part. The high value of m/H_G does not mean here that there is more hydrogen there, as mentioned by discussing **Figure 2**. In fact, this is the opposite. The value of H_D/H_G in the blue and red regions (not shown here) give typically values of 28 down to 17%, using the linear relation mentioned in Sect. 2.1. The zone where hydrogen has been outgassed displays a higher value of σ_G which is in agreement with what we know about the thermal stability of a-C:H [23, 49, 56]. The histograms of a TS deposit heated isothermally at 120°C for three times (120, 300 and 640 h) and at 250°C allows to show that the sample still evolve under long time scales (the average value of m/H_G increases slightly with time). The problem is that we need to average spectra on large zones because of large inhomogeneities found at the micrometric scale. However, using the mapping mode allows to identify different kind of defects of chemical environments which is needed to better characterize the sample. The average value of H_D/H_G (not shown here) leads to a value of H close to 20 %.

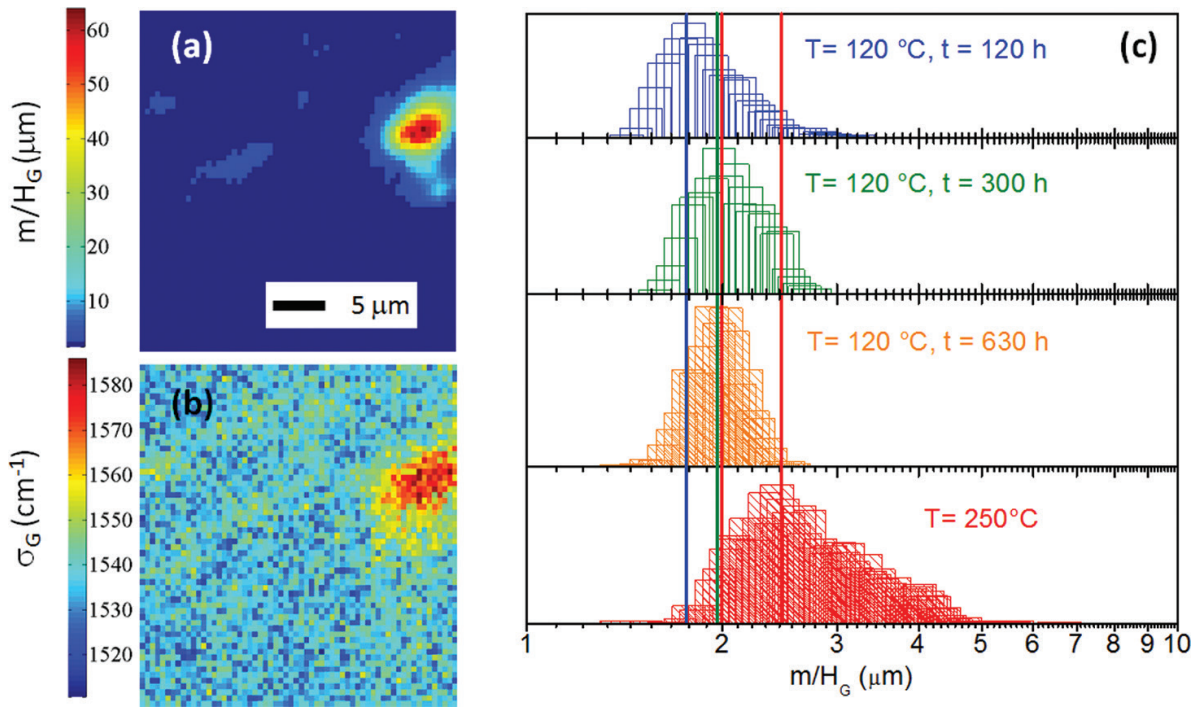


Figure 7. Raman spectroscopy imaging of a heated Tore Supra (TS) deposit. (a) m/H_G mapping of this TS sample. (b) σ_G mapping. (c) Histograms of heated TS samples (120°C during 120, 300 and 630 h, and 250°C).

2.3.3. Hydrogen depth concentration and history of Tore Supra deposits

In Ref. [72], lock-in thermography, scanning electron microscopy and confocal microscopy were used to study the erosion and depositions on the TPL of the Tore Supra tokamak. Taking into account, all the methods allowed the authors to perform a complete mapping of the mass of carbon that has been eroded and deposited. The findings were 520 g of deposits and 920 g of eroded carbon. It shows that more than a half of the carbon that is eroded is redeposited on the TPL. It was also found that the zones containing the highest deposits were found close to erosion zones.

Such things were simulated recently [31]. The gap deposition contribution is estimated at 23%, mostly from the erosion zones and with a main contribution from the low field side of the tile toroidal gap surfaces. This deuterium impoverishment in the deep layer has also been investigated more systematically in Ref. [73] where IBA and cross-section electron microscopy were done on 15 samples. The mean in-depth hydrogen isotope content is plotted in **Figure 8(b)** and scaled to the 120 μm of the deposit shown. The surface content has been divided by 2 in less than 20 μm . In parallel, σ_G is displayed for three lines of sight. Then on top of this deposit, the H content is close to 20%, whereas it decreases close to zero at the interface between the deposit and the top of the CFC. The diminution is rapid in the 20 first microns. Same trends are seen with the structure probed with Raman spectroscopy: carbon close to the surface is less organized (σ_G close to 1520 cm^{-1}), whereas σ_G increases (meaning an increase of order) and then reaches a plateau 20 μm deep in the deposit, at the value of $\sigma_G = 1580 \text{ cm}^{-1}$. This deuterium impoverishment of the deep layers may be caused by long-term release mechanisms, as discussed in the previous part.

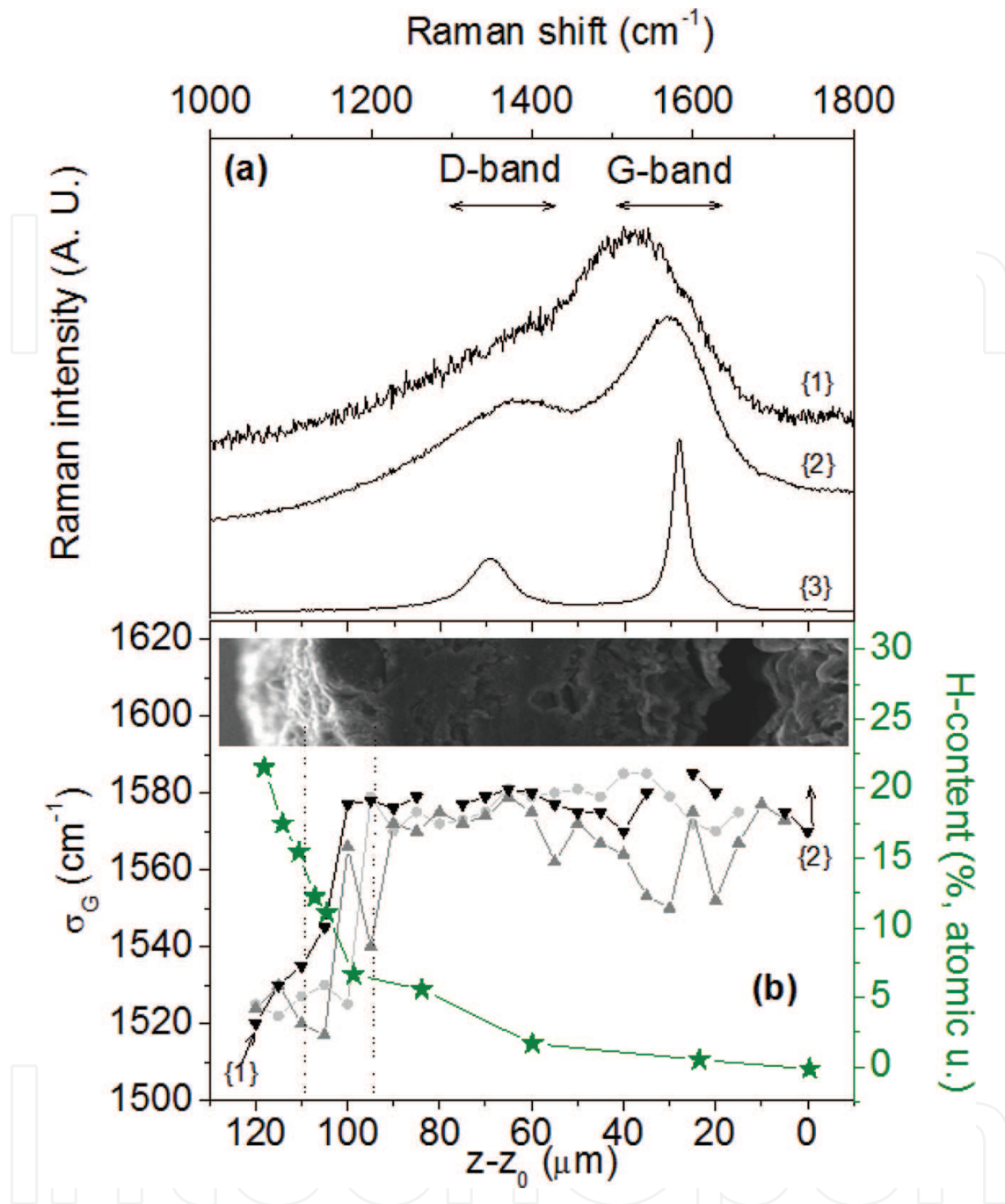


Figure 8. H-content impoverishment in deep deposits compared to ordering of the carbon. H content is extracted from Ref. [73].

3. Beryllium- and tungsten-based materials

3.1. Context

Tritium retention, occurring in a magnetically confined deuterium plus tritium plasma, can be obtained by erosion, retention, material modification, dust formation (and more generally plasma wall interactions). This is a big safety issue because of tritium radioactivity [7, 74].

Hydrogen isotope retention in beryllium can also play a role in the lifetime estimation of the ≈ 700 m² ITER's beryllium inner walls because of erosion [75]. This explains why several studies based on ion irradiation of Be samples have been devoted to D behavior to ensure that tritium retention will not be a limiting issue in ITER operations. Previous studies found D/Be ratio in the range 0.1–0.7 using energies in the range 0.6–20 keV/D and fluency in the range 10^{16} – 10^{19} cm⁻² [76–82].

At fluencies close to 2×10^{17} cm⁻² (in the range 0.6–1 keV/D), the existence of the D-content saturation (D/Be close to 0.25) has been shown [13, 83–84]. For fluencies lower than 0.7×10^{17} cm⁻² TDS display only one peak at 900 K, whereas for fluencies between 0.7 and 1×10^{17} cm⁻², a second peak lies at 750 K. For fluencies higher than 1.2×10^{17} cm⁻², two extra peak rise close to 500 K. These last peaks were explained by structural modification of the sample. Moreover, the role of crystal orientation and D diffusion along grain boundaries was investigated in [85]. The existence of BeH₂ was suggested in [17] but never observed before.

Raman microscopy is a nondestructive, noncontact and local (≈ 1 μ m² lateral resolution [86]) technique that has been proved to be sensitive to Be stretching modes [87], beryllium oxide modes [88], bending and stretching tungsten oxide modes [89], Be_xW_y-mixed samples density of states [90], BeCW-irradiated samples [91] and give information when a pristine material is implanted by hydrogen ions [90, 92, 93]. First Raman analyses in ILW-tokamaks were performed on some molybdenum JET mirrors [90], showing that the technique is sensitive to thin ≈ 10 nm deposited layer composed of $\approx 33\%$ Be, $\approx 33\%$ C and $\approx 33\%$ O and the underlying molybdenum oxidized mirror. C–O and C=O modes have been detected in that layer and defective or beryllium mixed with O and/or C have been found without possibility to identify the phases rigorously up to now, because of a poor benchmarking of the technique for these materials. Raman microscopy can also be able to give information about the hydrogen isotope behavior by combining IBA, Raman microscopy, atomic force microscopy (AFM) and with the help of DFT modeling. As an illustration of this complementarity, in Ref. [94], we identified on laboratory experiments the growth of BeD₂ with dendritic forms appearing subsequently to 2 keV ion implantation when the Be layer is saturated by implanted D ions. The width of the bands recorded by Raman microscopy suggested that this hydride has grown in a crystalline form which seems to be close to a body-centered orthorhombic structure with Ibam symmetry as the spectra look like to the ones reported in [95], who determined recently the structure by using additionally synchrotron X-ray diffraction. In [94], we showed that these dendrites appear when the amount of deuterium in the material is higher than $\approx 2 \times 10^{17}$ D.cm⁻², when the ≈ 40 nm under surface layer is saturated by D.

3.2. Laboratory experiments

3.2.1. Defect-induced bands in beryllium

Below, we compare defective Be samples that have been produced by Be deposits in an impurity atmosphere or by D implantation. In more details, the defective deposit sample has been produced by the thermionic vacuum (TVA) method (more details can be found in Ref. [96] and references therein). To introduce disorder, a partial pressure of N₂ (in the range from 10^{-2} to 10^{-3} Pa partial pressure) has been used during the deposit. The amount of N being ≈ 5 atomic %.

The D-implanted Be sample have been prepared with two impinging ion geometries, with 2 keV/D: normal incidence (90°) and 45° incidence. More details about the implantation of the 90° geometry can be found in [94].

Figure 9 displays Raman spectra of a deposited Be sample with a high content of defects for four laser wavelengths. Data were acquired with 633, 514, 488 and 325 nm lasers. The band associated to the E_{2G} Raman active mode is downshifted for the defective sample, but the shift depends on the wavelength. $\Gamma_{E_{2G}}$ for the reference sample is close to 8 cm^{-1} . For the defective sample, it is higher (27 cm^{-1}). The logarithmic scale used here allows to distinguish several additional broad bands ($413, 544$ and 616 cm^{-1}) that were first evidenced in Ref. [90] and called defect-induced bands. These bands are attributed to the phonon density of states (PDOS), as can be seen by comparing the Raman spectrum (where the E_{2G} band has been removed) to the PDOS of Be measured in the literature. Their intensity reaches values as high as 23% of the Raman active E_{2G} mode heights and they are related to the defect content, defect being a term which can be impurity, vacancy or other kind of defects.

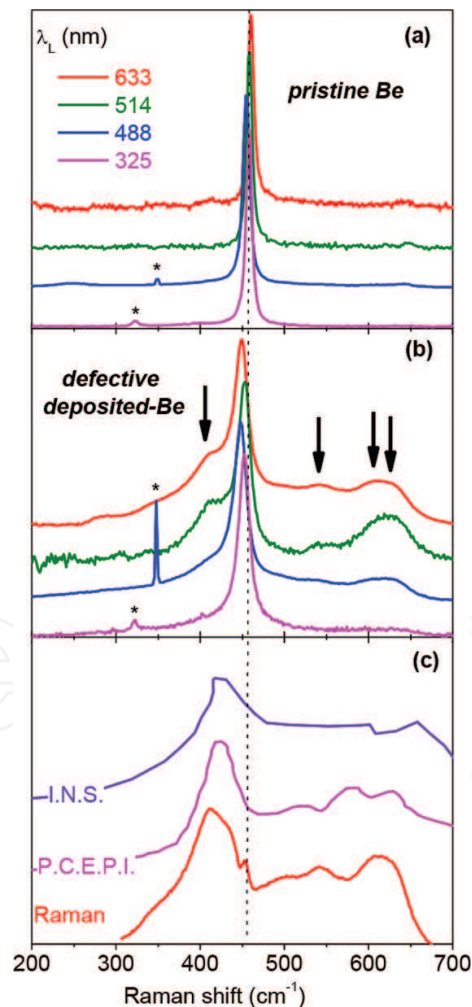


Figure 9. Normalized Raman spectra of a pristine (a) and defective (b) Be deposited sample, using four laser wavelength. (c) The 633 nm spectrum of the defective sample is displayed after removing the E_{2G} Raman active mode and is compared to the PDOS measured by INS and by PCEPI [97]. The bands marked by stars are due to other laser electronic transitions.

Changing the wavelength does not change the qualitative trends: the band related to the E_{2G} mode is more downshifted to low frequencies and broader. However, quantitative differences can also be seen, with some information. For example, the height of the PDOS diminishes monotonically with the decrease of the laser wavelength (from 23% with 633 nm down to 4% with 325 nm for the defective sample). $\sigma_{E_{2G}}$ does not display a monotonic evolution with the laser wavelength for the defective sample. The reference sample, oppositely, does not disperse in the range 325–633 nm. Shifts observed may then be due to stress [86] in the deposited layer, the nonmonotonic behavior being caused by two effects: stress gradients existing in the deposited layers and the penetration depth of the laser that is wavelength dependent.

In **Figure 10**, we compare 514 nm spectra of a pristine Be, a Be sample containing 2×10^{17} D cm^{-2} in the 90° geometry and 514 nm spectrum of Be sample in the 45° geometry. D implantation (**Figure 10(b)**) and vacancy creation profiles were evaluated for the 90° and 45° geometries

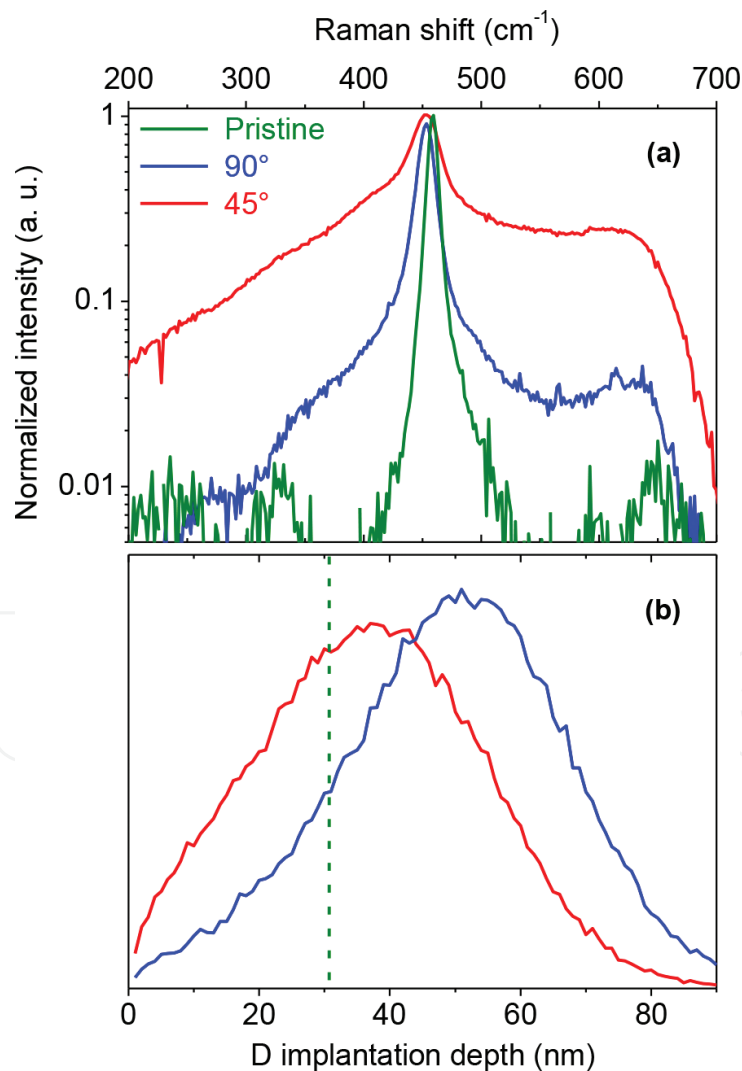


Figure 10. Varying the in-depth defects. (a) Normalized Raman spectra of D implanted Be samples. Geometry implantation (90° and 45°) are compared with the 514 nm laser wavelength.

using the stopping and range of ions in matter (SRIM) code² [68]. If we believe in SRIM calculations (which gives trends as many mechanisms and effects are not included), we can then estimate that 16% of the implanted deuterium atoms are implanted in the range 0–19 nm, 31% in the range 0–28 nm and 37% in the range 0–31 nm. For the corresponding ranges, the total amount of vacancies created are, respectively, 37, 59 and 65% of the total vacancies created. The lineal density of vacancies is the higher in the range 0–28 nm, being lower by 7.6% in the 0–19 nm range and by 0.4% in the 0–31 nm range.

We see that the Be implanted by D in the 90° geometry displays a Raman spectrum with a E_{2G} mode downshifted by 5 cm^{-1} and with an additional broadening of 6.5 cm^{-1} compared to the pristine sample. The PDOS is present, with a relative height ratio of $H_{\text{PDOS}}/H_{\text{Be}}=3\%$. If we compare with the Be implanted by D in the 45° geometry, we see that the band corresponding to the E_{2G} mode is downshifted by 5 cm^{-1} , with an additional broadening of 30 cm^{-1} compared to the pristine sample. The PDOS is rising, with a relative height ratio $H_{\text{PDOS}}/H_{\text{Be}}$ of 24%. The band position is the same in the two implantation geometries. However, the bandwidth Γ_{Be} is increased by a factor 2.7 and the PDOS relative height $H_{\text{PDOS}}/H_{\text{Be}}$ is increased by a factor 11 from the 90° to the 45° geometry. How these differences can be interpreted? According to SRIMS calculations in the subsurface slab going from 0 down to 31 nm, there are more defects (implanted D and vacancy) created in the 45° geometry than in the 90° geometry. Then, it explains why $H_{\text{PDOS}}/H_{\text{Be}}$ and Γ_{Be} are higher in the first case than in the second.

3.2.2. Characterization of Be nanometric hydrides

By using energetic ions, and with the help of nuclear reaction analysis (NRA), AFM, optical microscopy and quantum calculations compared to Raman spectroscopy, we were able to evidence the formation of crystalline BeD_2 [94]. The spectra are typically close to the one found for BeH_2 in Ref. [95] using high pressure to form them. It was shown previously that this latter technique is sensitive to the way hydrogen isotopes are bonded and organized in materials and thus that it can be relevant for fusion [92] and might be of interest for hydrogen storage by forming hydrides [98].

Figure 11 shows Raman imaging in the vicinity of a dendrite. In **Figure 11(c)**, the intensities of the band at 1397 cm^{-1} due to a Be-D mode are displayed. It is more intense on the dendrite and less intense off the dendrite. The corresponding spectra are displayed in **Figure 11(d)**. Details on how were obtained the spectra can be obtained in [94]. The bands marked by stars are due to Be-D bonds in BeD_2 . The fact that their corresponding intensity are higher are more intense on dendrite allows to conclude that the dendrites are made of BeD_2 . If the formation of such dendrites occurs in tokamaks, it could become a high fuel reservoir.

Figure 11(d) display the intensity of a mode found close to 1580 cm^{-1} and due to carbon contamination of the sample before it was bombarded (D and G bands in **Figure 11(e)**), and that has nothing to do with the experimental conditions.

²This code is widely used to investigate ion-surface interaction phenomena. It is a free access Monte-Carlo computer program based on the binary collision approximation that do not take into account crystal structure or vacancy diffusion (i.e. each single collision event is treated independently between two steps).

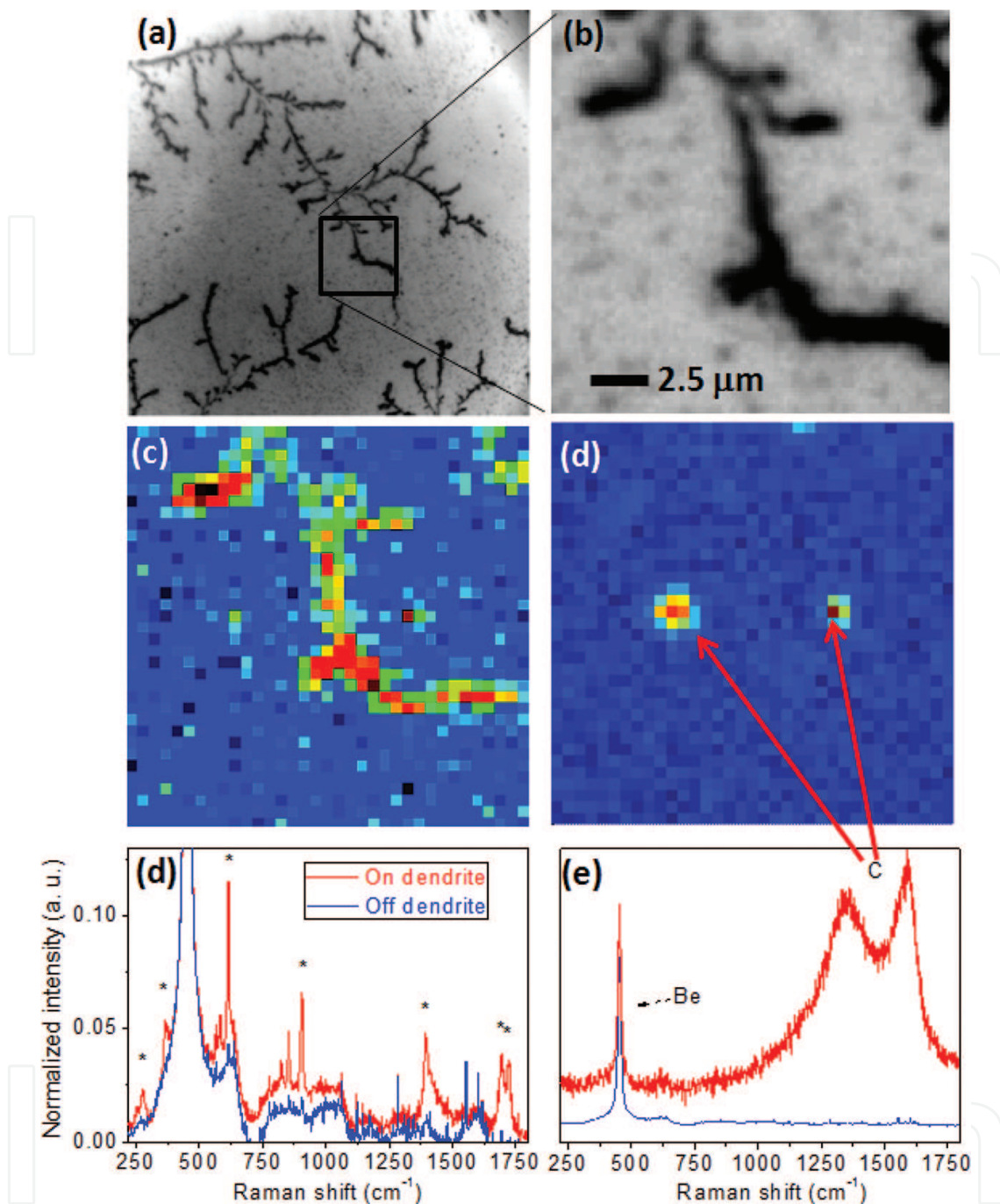


Figure 11. Beryllium hydride formation under ion implantation. (a) and (b) Optical microscopy. (c) Be-D bond intensity mapping. (d) Position of carbon impurities. (e) Comparison off/on dendrites. (f) Raman spectrum of carbon impurities.

3.2.3. Hydrogen behavior in tungsten oxide

Tungsten alone cannot be seen using standard Raman microscopy because there are no optical phonons that can be probed close to the center of the Brillouin zone. However, as oxygen is one of the impurities that can be found in tokamaks, and as the inner walls will be at temperatures ranging from few hundreds to 1000°C because of heat loads, it could be possible

that some oxide will be formed [99]. Then it would be of interest for the plasma-wall interaction community to take care of D and T behavior in tungsten oxides. Without entering into details, tungsten oxides can exist in various forms (dioxide, trioxide, in between stoichiometry), with many phase transitions that can be affected by nanosize effects [100] so that a systematic D implantation study could be helpful for the future. Today, only a few studies exist on the subject. In [93], we report on the formation of thin tungsten oxide layers that have been grown on W surfaces by thermal oxidation (thicknesses up to ~ 250 nm) and that have been exposed to low energy deuterium plasma (11 eV/D⁺). Raman microscopy and X-ray diffraction show a nanocrystalline WO₃ monoclinic structure. We observed that the low-energy deuterium plasma exposure has induced a phase transition, a change in the sample color and the formation of tungsten bronze (D_xWO₃). After exposure under ambient conditions, a reversible deuterium retention, due to oxidation of the D_xWO₃ layer, has been observed. **Figure 12** displays the effect of D implantation. The spectral range of tungsten trioxides can be roughly distributed in two kind of spectral regions: the bending modes region, lower than 500 cm⁻¹ and the stretching modes region at higher wavenumbers. Before exposure, we can see the characteristic peaks of the monoclinic structure at 703 and 805 cm⁻¹ which are attributed to symmetric and antisymmetric (O-W-O) stretching modes, respectively (see references in Ref. [93]). The wing in the range 920 – 970 cm⁻¹ is attributed to terminal oxygen bonding in case of nanocrystalline structures, but other interpretations can be found in the literature that we do not review here. Due to implantation, all the peaks are broadened, the bending modes display bands that are more intense than stretching modes, which can be the sign of some disorder, and two new bands appeared: one at 950 and the other at 388 cm⁻¹. These bands disappeared with time once put in air due to reoxydation.

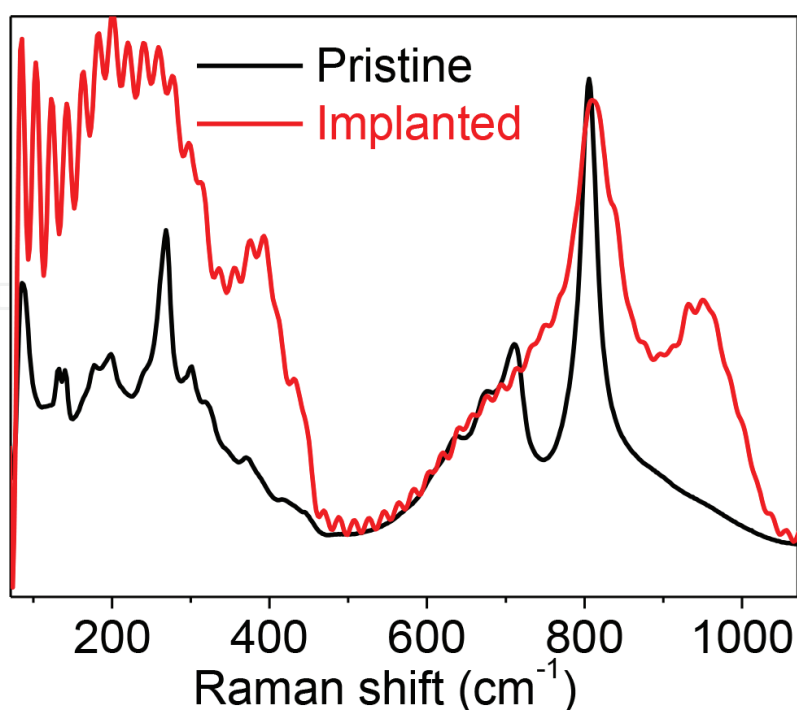


Figure 12. Raman spectra of bombarded WO₃.

4. Discussion/conclusion

Because of safety issue, it is important to understand how and where tritium will be stored in tokamaks due to plasma-wall interaction. In this chapter, we have demonstrated the ability of Raman microscopy to detect and characterize material changes subsequently to interaction with hydrogen, for both carbon-based tokamaks and for ITER-like wall materials (tungsten that is oxidized and beryllium). The comparison between well-controlled samples and sample extracted from tokamak has been used to better characterize some of the tokamaks' properties.

Among other findings, we report that by changing temperature on various carbon samples, extracted from tokamak (Tore Supra) or comparative reference laboratory samples (a-C:H) synthesized in controlled conditions, we have shown how Raman spectroscopic parameters can be used to characterize structural and H-content evolution/changes.

We also report that beryllium hydrides that can form high tritium reservoir in tokamaks can be formed and detected under ion implantation.

To conclude, next studies will have to use different laser wavelengths as they can be used to probe gradients of properties in the beryllium's depth due to the fact the depth probed is in the range of few tens of nanometer. This is the typical depth at which a high content of hydrogen isotope is found in modern tokamak samples like JET. Future studies have to be driven with this technique to better characterize the so-called supersaturated layer.

Author details

Cedric Pardanaud*, Celine Martin and Pascale Roubin

*Address all correspondence to: cedric.pardanaud@univ-amu.fr

Aix-Marseille Université/CNRS, Marseille, France

References

- [1] I.w. site, <https://www.iter.org/factsfigures>, in. ITER.org web site
- [2] R. Neu, A.U. Team, E.P. Taskforce, J.E. Contributors, Preparing the scientific basis for an all metal ITER, *Plasma Physics and Controlled Fusion*, 53 (2011) 124040.
- [3] V. Philipps, Tungsten as material for plasma-facing components in fusion devices, *Journal of Nuclear Materials*, 415 (2011) S2–S9.
- [4] F. Romanelli, I. Abel, V. Afanesyev, et al., Overview of the JET results with the ITER-like wall, *Nuclear Fusion*, 53 (2013) 104002.

- [5] S. Brezinsek, J.-E. Contributors, Plasma-surface interaction in the Be/W environment: Conclusions drawn from the JET-ILW for ITER, *Journal of Nuclear Materials*, 463 (2015) 11–21.
- [6] S. Brezinsek, A. Widdowson, M. Mayer, V. Philipps, P. Baron-Wiechec, J.W. Coenen, K. Heinola, A. Huber, J. Likonen, P. Petersson, M. Rubel, M.F. Stamp, D. Borodin, J.P. Coad, A.G. Carrasco, A. Kirschner, S. Krat, K. Krieger, B. Lipschultz, C. Linsmeier, G.F. Matthews, K. Schmid, J.E.T. Contributors, Beryllium migration in JET ITER-like wall plasmas, *Nuclear Fusion*, 55 (2015) 063021.
- [7] J. Roth, E. Tsitrone, A. Loarte, et al., Recent analysis of key plasma wall interactions issues for ITER, *Journal of Nuclear Materials*, 390-91 (2009) 1–9.
- [8] G.F. Matthews, J.E. Contributors, A.S.-U. Team, Plasma operation with an all metal first-wall: Comparison of an ITER-like wall with a carbon wall in JET, *Journal of Nuclear Materials*, 438 (2013) S2–S10.
- [9] I. Bykov, H. Bergsaker, G. Possnert, et al., Studies of Be migration in the JET tokamak using AMS with Be-10 marker, *Nuclear Instruments & Methods in Physics Research Section B-Beam Interactions with Materials and Atoms*, 371 (2016) 370–375.
- [10] K. Krieger, S. Brezinsek, M. Reinelt et al., Beryllium migration and evolution of first wall surface composition in the JET ILW configuration, *Journal of Nuclear Materials*, 438 (2013) S262–S266.
- [11] K. Schmid, M. Reinelt, K. Krieger, An integrated model of impurity migration and wall composition dynamics for tokamaks, *Journal of Nuclear Materials*, 415 (2011) S284–S288.
- [12] J. Likonen, K. Heinola, A. De Backer, S. Koivuranta, A. Hakola, C.F. Ayres, A. Baron-Wiechec, P. Coad, G.F. Matthews, M. Mayer, A. Widdowson, J. Contributors, Deuterium trapping and release in JET ITER-like wall divertor tiles, *Physica Scripta*, T167 (2016) 014074.
- [13] K. Heinola, A. Widdowson, J. Likonen, E. Alves, A. Baron-Wiechec, N. Barradas, S. Brezinsek, N. Catarino, P. Coad, S. Koivuranta, Long-term fuel retention in JET ITER-like wall, *Physica Scripta*, T167 (2016) 014075.
- [14] A. Kallenbach, M. Bernert, R. Dux, L. Casali, T. Eich, L. Giannone, A. Herrmann, R. McDermott, A. Mlynek, H.W. Mueller, F. Reimold, J. Schweinzer, M. Sertoli, G. Tardini, W. Treutterer, E. Viezzer, R. Wenninger, M. Wischmeier, A.U. Team, Impurity seeding for tokamak power exhaust: From present devices via ITER to DEMO, *Plasma Physics and Controlled Fusion*, 55 (2013) 124041.
- [15] M. Rubel, P. Petersson, E. Alves, S. Brezinsek, J.P. Coad, K. Heinola, M. Mayer, A. Widdowson, J.E.T. Contributors, The role and application of ion beam analysis for studies of plasma-facing components in controlled fusion devices, *Nuclear Instruments & Methods in Physics Research Section B-Beam Interactions with Materials and Atoms*, 371 (2016) 4–11.

- [16] P. Strom, P. Petersson, M. Rubel, A. Weckmann, S. Brezinsek, A. Kreter, S. Moeller, K. Rozniatowski, Characterisation of surface layers formed on plasma-facing components in controlled fusion devices: Role of heavy ion elastic recoil detection, *Vacuum*, 122 (2015) 260–267.
- [17] M. Reinelt, A. Allouche, M. Oberkofler, C. Linsmeier, Retention mechanisms and binding states of deuterium implanted into beryllium, *New Journal of Physics*, 11 (2009) 043023.
- [18] M. Reinelt, C. Linsmeier, Temperature programmed desorption of 1 keV deuterium implanted into clean beryllium, *Physica Scripta*, T128 (2007) 111–114.
- [19] M. Reinelt, C. Linsmeier, Ion implanted deuterium retention and release from clean and oxidized beryllium, *Journal of Nuclear Materials*, 390–91 (2009) 568–571.
- [20] R. Bisson, S. Markelj, O. Mourey, F. Ghiorghiu, K. Achkasov, J.M. Layet, P. Roubin, G. Cartry, C. Grisolia, T. Angot, Dynamic fuel retention in tokamak wall materials: An in situ laboratory study of deuterium release from polycrystalline tungsten at room temperature, *Journal of Nuclear Materials*, 467 (2015) 432–438.
- [21] C. Pardanaud, E. Areou, C. Martin, R. Ruffe, T. Angot, P. Roubin, C. Hopf, T. Schwarz-Selinger, W. Jacob, Raman micro-spectroscopy as a tool to measure the absorption coefficient and the erosion rate of hydrogenated amorphous carbon films heat-treated under hydrogen bombardment, *Diamond and Related Materials*, 22 (2012) 92–95.
- [22] T.W. Scharf, I.L. Singer, Thickness of diamond-like carbon coatings quantified with Raman spectroscopy, *Thin Solid Films*, 440 (2003) 138–144.
- [23] C. Pardanaud, C. Martin, G. Giacometti, N. Mellet, B. Pegourie, P. Roubin, Thermal stability and long term hydrogen/deuterium release from soft to hard amorphous carbon layers analyzed using in-situ Raman spectroscopy. Comparison with Tore Supra deposits, *Thin Solid Films*, 581 (2015) 92–98.
- [24] E. Tsitrone, C. Brosset, B. Pegourie, E. Gauthier, J. Bouvet, J. Bucalossi, S. Carpentier, Y. Corre, E. Delchambre, L. Desgranges, T. Dittmar, D. Douai, A. Ekedahl, A. Escarguel, P. Ghendrih, C. Grisolia, A. Grosman, J. Gunn, S.H. Hong, W. Jacob, F. Kazarian, M. Kocan, H. Khodja, F. Linez, T. Loarer, Y. Marandet, A. Martinez, M. Mayer, O. Meyer, P.M. Garbet, P. Moreau, J.Y. Pascal, B. Pasquet, F. Rimini, H. Roche, I. Roure, S. Rosanvallon, P. Roubin, J. Roth, F. Saint-Laurent, F. Samaille, S. Vartanian, Deuterium inventory in Tore Supra: Reconciling particle balance and post-mortem analysis, *Nuclear Fusion*, 49 (2009) 075011.
- [25] T. Dittmar, P. Roubin, E. Tsitrone, E. Gauthier, A. Hakola, J. Likonen, F. Linez, C. Martin, M. Mayer, C. Pardanaud, J.Y. Pascal, B. Pasquet, B. Pégourié, J. Roth, I. Roure, R. Ruffe, Deuterium inventory in Tore Supra: Status of post-mortem analyses, *Physica Scripta*, T138 (2009) 014027.
- [26] T. Dittmar, E. Tsitrone, B. Pegourie, I. Cadez, P. Pelicon, E. Gauthier, P. Languille, J. Likonen, A. Litnovsky, S. Markelj, C. Martin, M. Mayer, J.-Y. Pascal, C. Pardanaud, V. Philipps, J. Roth, P. Roubin, P. Vavpetic, Deuterium Inventory in Tore Supra (DITS):

2nd post-mortem analysis campaign and fuel retention in the gaps, *Journal Of Nuclear Materials*, 415 (2011) S757–S760.

- [27] C. Martin, B. Pegourie, R. Ruffe, Y. Marandet, G. Giacometti, C. Pardanaud, P. Languille, S. Panayotis, E. Tsitrone, P. Roubin, Structural analysis of eroded carbon fiber composite tiles of Tore Supra: Insights on ion transport and erosion parameters, *Physica Scripta*, T145 (2011) 4.
- [28] C. Pardanaud, G. Giacometti, C. Martin, R. Ruffe, T. Angot, E. Aréou, B. Pégourié, E. Tsitrone, T. Dittmar, C. Hopf, W. Jacob, T. Schwarz-Selinger, P. Roubin, Raman study of CFC tiles extracted from the toroidal pump limiter of Tore Supra, *Journal of Nuclear Materials*, 415 (2011) S254–S257.
- [29] C. Pardanaud, C. Martin, P. Roubin, Multiwavelength Raman spectroscopy analysis of a large sampling of disordered carbons extracted from the Tore Supra tokamak, *Vibrational Spectroscopy*, 70 (2014) 187–192.
- [30] N. Mellet, C. Martin, B. Pegourie, G. Giacometti, J.P. Gunn, G. Cartry, P. Languille, C. Pardanaud, S. Panayotis, G. Amiard, Y. Marandet, P. Roubin, Modelling of the micro-metric erosion pattern observed on the Tore Supra limiter tiles, *Nuclear Fusion*, 54 (2014).
- [31] S. Panayotis, B. Pegourie, D. Borodin, A. Kirschner, J. Gunn, Y. Marandet, N. Mellet, Modelling the erosion/deposition pattern of the Tore Supra toroidal pumped limiter, *Journal of Nuclear Materials*, 463 (2015) 827–831.
- [32] F. Tuinstra, J.L. Koenig, Raman spectrum of graphite, *Journal of Chemical Physics*, 53 (1970) 1126.
- [33] S. Piscanec, F. Mauri, A.C. Ferrari, M. Lazzeri, J. Robertson, Ab initio Raman spectra of diamond like carbons, *Diamond and Related Materials*, 14 (2005) 1078.
- [34] M.M. Lucchese, F. Stavale, E.H.M. Ferreira, C. Vilani, M.V.O. Moutinho, R.B. Capaz, C.A. Achete, A. Jorio, Quantifying ion-induced defects and Raman relaxation length in graphene, *Carbon*, 48 (2010) 1592–1597.
- [35] J. Schwan, S. Ulrich, V. Bathori, H. Erhardt, S.R.P. Silva, Raman spectroscopy on amorphous carbon films, *Journal of Applied Physics*, 80 (1996) 440–447.
- [36] E.H.M. Ferreira, M.V.O. Moutinho, F. Stavale, M.M. Lucchese, R.B. Capaz, C.A. Achete, A. Jorio, Evolution of the Raman spectra from single-, few-, and many-layer graphene with increasing disorder, *Physical Review B*, 82 (2010) 9.
- [37] A.C. Ferrari, J. Robertson, Resonant Raman spectroscopy of disordered, amorphous, and diamond like carbon, *Physical Review B*, 64 (2001) 075414.
- [38] C. Beny-Bassez, J.N. Rouzaud, Characterization of carbonaceous materials by correlated electron and optical microscopy and Raman microspectroscopy, *Scanning Electron Microscope*, 1 (1985) 119–132.
- [39] T. Jawhari, A. Roid, J. Casado, Raman spectroscopic characterization of some commercially available carbon black materials, *Carbon*, 33 (1995) 1561–1565.

- [40] A. Sadezky, H. Muckenhuber, H. Grothe, R. Niessner, U. Pöschl, Raman micro spectroscopy of soot and related carbonaceous materials: Spectral analysis and structural information, *Carbon*, 43 (2005) 1731–1742.
- [41] J.M. Vallerot, X. Bourrat, A. Mouchon, G. Chollon, Quantitative structural and textural assessment of laminar pyrocarbons through Raman spectroscopy, electron diffraction and few techniques, *Carbon*, 44 (2006) 1833–1844.
- [42] J. Wagner, M. Ramsteiner, C.H. Wild, P. Koidl, Resonant Raman scattering of amorphous carbon and polycrystalline diamond films, *Physical Review B*, 40 (1989) 1817–1824.
- [43] C. Pardanaud, C. Martin, G. Cartry, A. Ahmad, L. Schiesko, G. Giacometti, M. Carrere, P. Roubin, In-plane and out-of-plane defects of graphite bombarded by H, D and He investigated by atomic force and Raman microscopies, *Journal of Raman Spectroscopy*, 46 (2015) 256–265.
- [44] A.C. Ferrari, J. Robertson, Interpretation of Raman spectra of disordered and amorphous carbon, *Physical Review B*, 61 (2000) 14095.
- [45] J.G. Buijsters, R. Gago, I. Jiménez, M. Camero, F. Agullo-Rueda, C. Gomez-Aleixandre, Hydrogen quantification in hydrogenated amorphous carbon films by infrared, Raman, and X-ray absorption near edge spectroscopies, *Journal of Applied Physics*, 105 (2009) 093510.
- [46] C. Casiraghi, A.C. Ferrari, J. Robertson, Raman spectroscopy of hydrogenated amorphous carbons, *Physical Review B*, 72 (2005) 085401.
- [47] C. Pardanaud, C. Martin, P. Roubin, G. Giacometti, C. Hopf, T. Schwarz-Selinger, W. Jacob., Raman spectroscopy investigation of the H content of heated hard amorphous carbon layers, *Diamond and Related Materials*, 34 (2013) 100–104.
- [48] A.C. Ferrari, J. Robertson, Interpretation of Raman spectra of disordered and amorphous carbon, *Physical Review B*, 61 (2000) 14095–14107.
- [49] C. Pardanaud, C. Martin, P. Roubin, G. Giacometti, C. Hopf, T. Schwarz-Selinger, W. Jacob, Raman spectroscopy investigation of the H content of heated hard amorphous carbon layers, *Diamond and Related Materials*, 34 (2013) 100–104.
- [50] T. Schwarz-Selinger, A. von Keudell, W. Jacob, Plasma chemical vapor deposition of hydrocarbon films: The influence of hydrocarbon source gas on the film properties, *Journal of Applied Physics*, 86 (1999) 3988–3996.
- [51] C. Wild, P. Koidl, Thermal gas effusion from hydrogenated amorphous-carbon films, *Applied Physics Letter*, 51 (1987) 1506–1508.
- [52] J. Ristein, R.T. Stief, L. Ley, W. Beyer, A comparative analysis of a-C : H by infrared spectroscopy and mass selected thermal effusion, *Journal of Applied Physics*, 84 (1998) 3836–3847.
- [53] E. Salançon, T. Dürbeck, T. Schwarz-Selinger, F. Genoese, W. Jacob, Redeposition of amorphous hydrogenated carbon films during thermal decomposition, *Journal of Nuclear Materials*, 376 (2008) 160.

- [54] H. Ito, K. Yamamoto, M. Masuko, Thermal stability of UBM sputtered DLC coatings with various hydrogen contents, *Thin Solid Films*, 517 (2008) 1115–1119.
- [55] J.G. Buijnsters, R. Gago, A. Redondo-Cubero, I. Jimenez, Hydrogen stability in hydrogenated amorphous carbon films with polymer-like and diamond-like structure, *Journal of Applied Physics*, 112 (2012) 093502.
- [56] C. Pardanaud, C. Martin, G. Giacometti, P. Roubin, B. Pegourie, C. Hopf, T. Schwarz-Selinger, W. Jacob, J.G. Buijnsters, Long-term H-release of hard and intermediate between hard and soft amorphous carbon evidenced by in situ Raman microscopy under isothermal heating, *Diamond and Related Materials*, 37 (2013) 92–96.
- [57] R. Coratger, A. Claverie, A. Chahboun, V. Landry, F. Ajustron, J. Beauvillain, Effects of ion mass and energy on the damage induced by an ion beam on graphite surfaces: A scanning tunneling microscopy study, *Surface Science*, 262 (1992) 208–218.
- [58] B. An, S. Fukuyama, K. Yokogawa, M. Yoshimura, Evolution of Ar⁺-damaged graphite surface during annealing as investigated by scanning probe microscopy, *Journal of Applied Physics*, 92 (2002) 2317–2322.
- [59] V.F. Elesin, L.A. Openov, Clusters of interstitial carbon atoms near the graphite surface as a possible origin of dome-like features observed by scanning tunneling microscopy, *Surface Science*, 442 (1999) 131–140.
- [60] B.S. Elman, M. Shayegan, M.S. Dresselhaus, H. Mazurek, G. Dresselhaus, Structural characterization of ion-implanted graphite, *Physical Review B*, 25 (1982) 4142.
- [61] M. Kappel, J. Küppers, Ripening of subsurface amorphous C clusters formed by low energy He ion bombardment of graphite, *Surface Science*, 440 (1999) 387–397.
- [62] M. Kappel, M. Steidl, J. Biener, J. Küppers, Surface topography of low energy He-ion-bombarded graphite by AFM: Temperature effects, *Surface Science Letters*, 387 (1997) L1062–L1067.
- [63] T.L. Makarova, A.L. Shelankov, I.T. Serenkov, V.I. Sakharov, D.W. Boukhvalov, Anisotropic magnetism of graphite irradiated with medium-energy hydrogen and helium ions, *Physical Review B*, 83 (2011) 085417.
- [64] K. Niwase, Irradiation-induced amorphisation of graphite, *Physical Review B*, 52 (1995) 15785–15798.
- [65] K. Nordlund, J. Keinonen, T. Mattila, Formation of ion irradiation induced small-scale defects on graphite surfaces, *Physical Review Letter*, 77 (1996) 699.
- [66] P.J. Zhai, Y.X. Xing, Y. Zhang, S.L. Feng, Y.X. Kang, X.W. Tang, Y.G. Wang, W.J. Zhao, S. Yan, Observation and study of latent tracks on the surface of HOPG induced by H⁺ ions, *Radiation Measurements*, 28 (1997) 97–100.
- [67] H. Zhang, M. Zhao, X. Yang, H. Xia, X. Liu, Y. Xia, Diffusion and coalescence of vacancies and interstitials in graphite: A first-principles study, *Diamond and Related Materials*, 19 (2010) 1240–1244.

- [68] J.F. Ziegler, J.P. Biersack, U. Littmark, *The Stopping and Range of Ions in Matter*, Pergamon, New York, 1995.
- [69] C. Martin, R. Ruffe, C. Pardanaud, M. Cabié, C. Dominici, T. Dittmar, P. Languille, B. Pegourié, E. Tsitrone, P. Roubin, Structure of the carbon layers deposited on the toroidal pump limiter of Tore Supra, *Journal of Nuclear Materials*, 415 (2011) S258–S261.
- [70] M. Richou, C. Martin, P. Delhaes, M. Couzi, W. Saikaly, C. Brosset, B. Pégourié, A. Litnovsky, V. Philipps, P. Wienhold, J. Dentzer, C. Vix-Guterl, P. Roubin, Physico-chemical characteristics of carbon deposits collected in TEXTOR and Tore Supra tokamaks, *Carbon*, 45 (2007) 2723–2731.
- [71] S. Panayotis, B. Pegourie, E. Caprin, D. Douai, J.-C. Hatchressian, V. Negrier, J.-Y. Pascal, S. Vartanian, J. Bucalossi, P. Monier-Garbet, Deuterium inventory in Tore Supra: Contribution of carbon deposits outgassing, *Journal of Nuclear Materials*, 438 (2013) S1059–S1062.
- [72] C. Martin, P. Languille, S. Panayotis, B. Pegourie, H. Roche, C. Pardanaud, G. Giacometti, R. Ruffe, E. Gauthier, X. Courtois, E. Tsitrone, P. Roubin, Erosion-deposition mapping of the toroidal pump limiter of Tore Supra, *Journal of Nuclear Materials*, 438 (2013) S771–S774.
- [73] B. Pegourie, S. Panayotis, P. Languille, C. Martin, T. Dittmar, E. Gauthier, J.-C. Hatchressian, J.-Y. Pascal, P. Roubin, R.T. Ruffe, E., S. Vartanian, H. Wang, A. Beaute, J. Bouvet, C. Brosset, J. Bucalossi, M. Cabie, E. Caprin, X. Courtois, R. Dachicourt, E. Delchambre, C. Dominici, D. Douai, A. Ekedahl, J.P. Gunn, A. Hakola, W. Jacob, H. Khodja, J. Likonen, F. Linez, A. Litnovsky, Y. Marandet, S. Markelj, A. Martinez, M. Mayer, O. Meyer, P. Monier-Garbet, P. Moreau, V. Negrier, P. Oddon, C. Pardanaud, B. Pasquet, P. Pelicon, P. Petersson, V. Philipps, G. Possnert, D. Reiter, J. Roth, I. Roure, M. Rubel, F. St-Laurent, F. Samaille, P. Vavpetic, Deuterium inventory in Tore Supra: Coupled carbon-deuterium balance, *Journal of Nuclear Materials*, 438 (2013) S120–S125.
- [74] J. Roth, E. Tsitrone, A. Loarte, Plasma-wall interaction: Important ion induced surface processes and strategy of the EU Task Force, *Nuclear Instruments & Methods in Physics Research Section B-Beam Interactions with Materials and Atoms*, 258 (2007) 253–263.
- [75] D. Borodin, S. Brezinsek, J. Miettunen, M. Stamp, A. Kirschner, C. Bjorkas, M. Groth, S. Marsen, C. Silva, S.W. Lisgo, D. Matveev, M. Airila, V. Philipps, J.-E. Contributors, Determination of Be sputtering yields from spectroscopic observations at the JET ITER-like wall based on three-dimensional ERO modelling, *Physica Scripta*, T159 (2014) 014057.
- [76] G. De Temmerman, M.J. Baldwin, R.P. Doerner, D. Nishijima, K. Schmid, An empirical scaling for deuterium retention in co-deposited beryllium layers, *Nuclear Fusion*, 48 (2008) 075008.
- [77] G. De Temmerman, R.P. Doerner, Revised scaling equation for the prediction of tritium retention in beryllium co-deposited layers, *Nuclear Fusion*, 49 (2009) 042002.
- [78] M. Mayer, R. Behrisch, H. Plank, J. Roth, G. Dollinger, C.M. Frey, Codeposition of hydrogen with beryllium, carbon and tungsten, *Journal of Nuclear Materials*, 230 (1996) 67–73.

- [79] R.A. Causey, D.S. Walsh, Codeposition of deuterium with beryllium, *Journal of Nuclear Materials*, 254 (1998) 84–86.
- [80] M.J. Baldwin, K. Schmid, R.P. Doerner, A. Wiltner, R. Seraydarian, C. Linsmeier, Composition and hydrogen isotope retention analysis of co-deposited C/Be layers, *Journal of Nuclear Materials*, 337 (2005) 590–594.
- [81] J.T. Zhao, Q. Wang, T.S. Wang, X.X. Xu, S. Zhang, Y.S. Zhou, X.C. Guan, K.H. Fang, J. Kasagi, Dynamical saturated concentration of deuterium in a beryllium foil studied by low energy D(d,p)T reaction, *Nuclear Instruments & Methods in Physics Research Section B-Beam Interactions with Materials and Atoms*, 316 (2013) 13–16.
- [82] V.K. Alimov, V.N. Chernikov, A.P. Zakharov, Depth distribution of deuterium atoms and molecules in beryllium implanted with D ions, *Journal of Nuclear Materials*, 241 (1997) 1047–1051.
- [83] M. Oberkofler, C. Linsmeier, Deuterium release from implanted beryllium and beryllium oxide, *Journal of Nuclear Materials*, 415 (2011) S724–S727.
- [84] A.A. Haasz, J.W. Davis, Deuterium retention in beryllium, molybdenum and tungsten at high fluences, *Journal of Nuclear Materials*, 241 (1997) 1076–1081.
- [85] R. Piechoczek, M. Reinelt, M. Oberkofler, A. Allouche, C. Linsmeier, Deuterium trapping and release in Be(0001), Be(11-20) and polycrystalline beryllium, *Journal of Nuclear Materials*, 438 (2013) S1072–S1075.
- [86] G. Gouadec, P. Colomban, Raman spectroscopy of nanomaterials: How spectra relate to disorder, particle size and mechanical properties, *Progress in Crystal Growth and Characterization of Materials*, 53 (2007) 1–56.
- [87] W.J. Evans, M.J. Lipp, H. Cynn, C.S. Yoo, M. Somayazulu, D. Hausermann, G. Shen, V. Prakapenka, X-ray diffraction and Raman studies of beryllium: Static and elastic properties at high pressures, *Physical Review B*, 72 (2005).
- [88] G. Morell, W. Perez, E. ChingPrado, R.S. Katiyar, An harmonic interactions in beryllium oxide, *Physical Review B*, 53 (1996) 5388–5395.
- [89] M. Boulova, N. Rosman, P. Bouvier, G. Lucazeau, High-pressure Raman study of microcrystalline WO₃ tungsten oxide, *Journal of Physics-Condensed Matter*, 14 (2002) 5849–5863.
- [90] C. Pardanaud, M.I. Rusu, G. Giacometti, C. Martin, Y. Addab, P. Roubin, C.P. Lungu, C. Porosnicu, I. Jepu, P. Dinca, M. Lungu, O.G. Pompilian, R. Mateus, E. Alves, M. Rubel, J. contributors, Raman microscopy investigation of beryllium materials, *Physica Scripta*, T167 (2016) 014027.
- [91] L. Avotina, A. Marcu, C. Porosnicu, M. Lungu, A. Stancalie, A.G. Ilie, P.C. Ganea, D. Savastru, J. Kalnacs, C.P. Lungu, G. Kizane, S. Antohe, Multi-wavelength laser irradiation of Be-C-W coatings, *Digest Journal of Nanomaterials and Biostructures*, 11 (2016) 293–302.

- [92] C. Pardanaud, Y. Addab, C. Martin, P. Roubin, B. Pegourié, M. Oberkofler, M. Köppen, T. Dittmar, C. Linsmeier, Raman microscopy as a defect microprobe for hydrogen bonding characterization in materials used in fusion applications, *Physica Status Solidi (c)*, 12 (2015) 98–101.
- [93] Y. Addab, C. Martin, C. Pardanaud, J. Khayadjian, K. Achkasov, D. Kogut, G. Cartry, G. Giacometti, M. Cabié, J.L. Gardarein, Formation of thin tungsten oxide layers: Characterization and exposure to deuterium, *Physica Scripta*, T167 (2016) 014036.
- [94] C. Pardanaud, M.I. Rusu, C. Martin, G. Giacometti, P. Roubin, Y. Ferro, A. Allouche, M. Oberkofler, M. Köppen, T. Dittmar, C. Linsmeier, Hydrogen retention in beryllium: Concentration effect and nanocrystalline growth, *Journal of Physics: Condensed Matter*, 27 (2015) 475401.
- [95] C. Pépin, P. Loubeyre, Layered structure and re-entrant disproportionation observed in crystalline BeH₂ under pressure, *Physical Review B*, 93 (2016) 224104.
- [96] C.P. Lungu, C. Porosnicu, I. Jepu, M. Lungu, A. Marcu, C. Luculescu, C. Ticos, A. Marin, C.E.A. Grigorescu, The behavior of W, Be and C layers in interaction with plasma produced by terawatt laser beam pulses, *Vacuum*, 110 (2014) 207–212.
- [97] A.V. Khotkevich, I.K. Yanson, Atlas of point contact spectra of electron-phonon interactions in metals, Springer, 1995 springer Science+Business Media, New York, 978-0-7923-9526-3, DOI:10.1007/978-1-4615-2265-2
- [98] D. Reed, D. Book, Recent applications of Raman spectroscopy to the study of complex hydrides for hydrogen storage, *Current Opinion in Solid State & Materials Science*, 15 (2011) 62–72.
- [99] A. Pezzoli, D. Dellasega, V. Russo, A. Gallo, P.A.Z. van Emmichoven, M. Passoni, Thermal annealing and exposure to divertor-like deuterium plasma of tailored tungsten oxide coatings, *Journal of Nuclear Materials*, 463 (2015) 1041–1044.
- [100] T. Pagnier, M. Boulova, N. Sergent, P. Bouvier, G. Lucazeau, Nanopowders and nanostructured oxides: Phase transitions and surface reactivity, *Journal of Raman Spectroscopy*, 38 (2007) 756–761.